Carbohydrate Polymers 337 (2024) 122161

Contents lists available at ScienceDirect

Carbohydrate Polymers

journal homepage: www.elsevier.com/locate/carbpol

Chitosan-based electroconductive inks without chemical reaction for cost-effective and versatile 3D printing for electromagnetic interference (EMI) shielding and strain-sensing applications

Naresh D. Sanandiya [a], Avinash R. Pai [b], Shayan Seyedin [a], Fengzai Tang [c], Sabu Thomas [b], Fengwei Xie [a,d,*]

[a] School of Engineering, Newcastle University, Newcastle upon Tyne NE1 7RU, United Kingdom
[b] International and Inter University Centre for Nanoscience and Nanotechnology, Mahatma Gandhi University, Kottayam, Kerala 686560, India
[c] WMG, University of Warwick, Coventry, United Kingdom
[d] Department of Chemical Engineering, University of Bath, Bath BA2 7AY, United Kingdom

ARTICLE INFO

Original content: Data from research to develop chitosan-based electroconductive inks for 3D printing for EMI shielding and strain sensing applications (Original data)

Keywords:
Chitosan silk protein blend
Biopolymer DIW ink
EMI shielding material
Biopolymer composite materials
Biopolymer 3D printing
Biopolymer ink rheological properties

ABSTRACT

The burgeoning interest in biopolymer 3D printing arises from its capacity to meticulously engineer tailored, intricate structures, driven by the intrinsic benefits of biopolymers—renewability, chemical functionality, and biosafety. Nevertheless, the accessibility of economical and versatile 3D-printable biopolymer-based inks remains highly constrained. This study introduces an electroconductive ink for direct-ink-writing (DIW) 3D printing, distinguished by its straightforward preparation and commendable printability and material properties. The ink relies on chitosan as a binder, carbon fibers (CF) a low-cost electroactive filler, and silk fibroin (SF) a structural stabilizer. Freeform 3D printing manifests designated patterns of electroconductive strips embedded in an elastomer, actualizing effective strain sensors. The ink's high printability is demonstrated by printing complex geometries with porous, hollow, and overhanging structures without chemical or photoinitiated reactions or support baths. The composite is lightweight (density 0.29 ± 0.01 g/cm^3), electroconductive (2.64 ± 0.06 S/cm), and inexpensive (20 USD/kg), with tensile strength of 20.77 ± 0.60 MPa and Young's modulus of 3.92 ± 0.06 GPa. 3D-printed structures exhibited outstanding electromagnetic interference (EMI) shielding effectiveness of 30–31 dB, with shielding of >99.9 % incident electromagnetic waves, showcasing significant electronic application potential. Thus, this study presents a novel, easily prepared, and highly effective biopolymer-based ink poised to advance the landscape of 3D printing technologies.

1. Introduction

The exponential growth in the utilization of electronic devices has resulted in escalating levels of electromagnetic interference (EMI), posing significant threats to the performance of commercial and military electronic equipment. To mitigate EMI pollution, there is a need of highly efficient EMI-shielding materials, ideally with high magnetic permeability or electrical conductivity. Conventionally, various conductive metallic materials such as sheets, coatings, or films have been used for EMI shielding. However, these materials come with drawbacks such as high density, susceptibility to corrosion, and high cost, thereby limiting their applicability in the contemporary electronic landscape. Conversely, conductive polymer composites, composed of polymers substrate and electrically conductive fillers, have garnered notable attention due to its low density, flexibility, cost-effectiveness, and corrosion-resistance. Notably, the use of biopolymer — polymers derived from nature sources — to develop conductive composites has gained tremendous attention. This approach promotes sustainability and reduces reliance on petroleum-based materials, aligning with the growing global emphasis on eco-friendly solutions.

Various materials, including metals and carbon-based substances, have been employed for EMI-shielding purposes. However, they all come with drawbacks such as high cost and manufacturing complexity (see Table S1 for comparison), which limit their versatility for widespread applications. Recently, various biopolymer-based conductive materials for EMI-shielding applications have been explored, such as

* Corresponding author at: School of Engineering, Newcastle University, Newcastle upon Tyne NE1 7RU, United Kingdom.
E-mail addresses: david.xie@newcastle.ac.uk, dx335@bath.ac.uk (F. Xie).

https://doi.org/10.1016/j.carbpol.2024.122161
Received 1 December 2023; Received in revised form 19 February 2024; Accepted 11 April 2024
Available online 15 April 2024

cellulose/carbon nanofibers (CF), cellulose/carbon nanotubes (CNT), chitosan/MXene, chitosan/CNT, chitosan/CNT/$Ti_3C_2T_x$, chitosan/graphene oxide (GO)/iron particles (IP), and alginate/graphene (summarized in Table S2). However, most of these materials consist of expensive conductive fillers and require high-tech facilities for production, rendering them expensive for large-scale manufacturing and impeding their practical application. Furthermore, the structure and shapes of shields fabricated via foaming, film-casting, or compression molding are challenging to control, thereby restricting the applicability of these traditional methods, especially in industries such as aerospace that necessitate complex, three-dimensional, and controllable structures using advanced equipment. To obviate the aforementioned anomalies, additive manufacturing, also known as 3D printing, presents a straightforward yet groundbreaking fabrication method.

In recent years, 3D printing has become a focus of research because of its ability to additively create personalized or customized complex 3D structures with high accuracy to meet diverse application needs that traditionally manufactured articles cannot meet. Common biopolymers such as chitosan (Sanandiya, Vijay, Dimopoulou, Dritsas, & Fernandez, 2018), alginate (Iglesias-Mejuto & García-González, 2021), cellulose (Holland, Tuck, & Foster, 2018; Xu, Chai, Huang, & Markwald, 2012), gelatin (Madaghiele et al., 2014; Stein, Saathoff, Antoni, & Schlaefer, 2015), and starch (Liu, Chen, Zheng, Xie, & Chen, 2020; Zheng, Tang, Xie, & Chen, 2022) have been widely explored across various 3D printing techniques, such as direct ink writing (DIW), fused deposition modeling (FDM), inkjet modeling (IJM), projection micro-stereolithography (PμSL), binder jetting, and selective laser sintering (SLS). Among these different techniques, DIW stands out as one of the most popular, as it allows easy and reliable printing of 3D objects through the layer-by-layer deposition of material extruded by a pneumatic, screw, or piston mechanism without the use of masking. Commonly used DIW printers are highly portable and do not require additional equipment to fit into confined spaces. However, hydrogels utilized in DIW may require fast gelation, UV curability, self-healing capabilities, or tunable mechanical properties.

Alginate, owing to its unique ability to crosslink with multivalent metal cations such as Ca^{2+}, is the predominant biopolymer employed in DIW 3D printing (Liu et al., 2022). Biopolymers lacking inherent crosslinking properties can be extruded as pastes but usually exhibit low yield stress, leading to poor shape fidelity or even rendering them non-printable. Therefore, these biopolymers typically require chemical modification to tailor the printability of the inks (Xie, 2023). For example, chitosan/hydroxyapatite hydrogels necessitate thermal gelation (Demirtaş, Irmak, & Gümüşderelioğlu, 2017), nanocellulose relies on ionic crosslinking (Cernencu et al., 2019), and gellan gum and gelatin hydrogels require covalent crosslinkers (Keller, Stevens, & Wallace, 2016). Additionally, for post-extrusion curing, hydrogels need to be functionalized with acrylate groups for UV curing (Suo et al., 2018). Moreover, recently, there have been a proliferation of biopolymer-based 3D printable conductive inks. However, most of these formulations rely on a high concentration of electroconductive nanomaterials and require extensive chemical modification, in addition to the post-printing process mentioned above. These factors potentially contribute to their high cost and toxicity for large-scale manufacturing and hinder their practical applications (Table S3).

Here, we report on our development of chitosan-based electroconductive inks for versatile and cost-effective printing of constructs for EMI shielding, without the need for chemical reactions. The rationale to use chitosan, a polymer derived from chitin — the second most abundant biopolymer on Earth — is rooted in its widespread availability across diverse ecosystems (e.g., crustaceans, insects, fungi, and fish) and its scalability for manufacturing even at large scales (Dritsas, Halim, Vijay, Sanandiya, & Fernandez, 2018). However, the bottom-up use of chitosan for 3D printing is still plagued with problems (e.g., poor mechanical properties, uncontrolled shrinkage, poor shape retention, and post-processing requirements) that impede its application. Interestingly, in nature, a synergy between chitin and protein at the molecular level in insect wings (Vincent & Wegst, 2004) and crustaceans results in lightweight load-bearing structures with excellent shape-retention (Du et al., 2019). Inspired by these natural structures, in this study, we adopted a biomimetic approach to formulate 3D printable composites. Here, chitosan interacts with a β-sheet protein to enhance structural stability, mirroring the principles observed in natural systems (Vincent & Wegst, 2004).

Our hypothesis in this work is that chitosan, carbon fiber (CF), and silk protein (SF) can physically interact with each other to form a DIW ink with suitable rheological properties and a stabilized microstructure. We chose EMI shielding as an application case study here, considering that the production of traditional metal-based EMI-shielding materials could be resource-intensive and may also pose end-of-life management issues, while EMI shielding is increasingly needed nowadays due to the growing use of electronic devices. The challenges associated with traditional EMI-shielding frames could be potentially addressed by chitosan-based EMI-shielding materials and constructs developed in this work. These constructs exhibit comparable EMI-shielding performance while offering advantages such as lightweight, high mechanical strength, and toughness. Besides, the chitosan-based electroconductive inks can be easily printed into strips embedded in a silicone elastomer to create cost-effective strain sensors. Thus, we envision that the chitosan-based inks for freeform printing developed in this work, with their novelty showcased by their straightforward preparation, cost-effectiveness without the need for expensive conductive materials, lack of requirements for a supporting bath and post-printing crosslinking strategies, and excellent shape retention capability — attributes not achievable with current state-of-the-art methods — can offer valuable insights into the advancement of various non-chemically derived polymer inks. Moreover, they have the potential to expand the application of biopolymers in creating sustainable, disposable, and customized complex constructs for a multitude of applications.

2. Experimental

2.1. Materials

Milled carbon fiber (CF) powder was purchased from Easy Composite Ltd. (UK) (0.2 % moisture content). Acetic acid, hydrochloric acid (HCl), and sodium hydroxide (NaOH) of AR grade were purchased from Fisher Scientific (UK). Silk fibroin (SF), originally from *Bombyx mori*, with a molecular mass of 250,000 g/mol, was supplied by Huzhou Xintiansi Bio-tech Co., Ltd. (China) (3.9 % moisture content) and was used as received.

2.2. Extraction of chitin and deacetylation of chitin from seafood waste

The chitosan used in this study was produced in the lab by extracting chitin from prawn shells through a stepwise process of demineralization and deproteinization followed by deacetylation (Pakizeh, Moradi, & Ghassemi, 2021). Specifically, chitin was extracted from king prawn shells (*Penaeus monodon*) collected as food waste from a local seafood restaurant (Saltwater Fish Company, Newcastle upon Tyne, UK). The shells were washed with water to remove impurities and unwanted residues, followed by drying in an oven with controlled conditions of 40 °C for 24 h. The shells were then demineralized using 2 N HCl at a ratio of 1:5 (*w/v*) at a temperature of 30 °C for 2 h. To obtain purified chitin, deproteinization was carried out by treating the shells with 2 M NaOH at a ratio of 1:5 (w/v) at 60 °C for three cycles for 2 h per cycle (Fig. S1). The treated shells were then washed with deionized water to neutral pH and ground into 2–4 mm particles. The purity of chitin was ascertained by FTIR spectroscopy (Table S4 and Fig. S2) and solid-state ^{13}C NMR spectroscopy (Fig. S3).

For the deacetylation to obtain chitosan, the chitin was treated with a 20 % NaOH solution at a ratio of 1:10 (*w/v*) for 8 h at 120 °C in a three-

necked round-bottom flask equipped with a thermometer. The resulting chitosan slurry was filtered and washed with deionized water to a neutral pH. The chitosan was then dried in an oven with controlled conditions of 40 °C for 12 h and stored in a zip-lock bag for further use.

The molecular weight of the extracted chitosan was determined to be 138.18 kDa using an Ostwald viscometer. Four different concentrations (0.1–0.4 w/v) of chitosan solution were prepared in a solvent mixture of 0.2 M acetic acid and 0.2 M sodium acetate (1:1). The intrinsic viscosity values were utilized in the Mark-Houwink equation, as shown in the following equation (Eq. (1)), to determine the molecular weight.

$$[\eta] = K\,M^{\alpha} \tag{1}$$

where $[\eta]$ is intrinsic viscosity, M is molecular weight, and K and α are Mark-Houwink constants (Sanandiya et al., 2020).

2.3. Preparation of conductive composites and 3D printing inks

Chitosan solutions of 5–15 % *w*/w concentrations were prepared by dissolving specific amounts of chitosan in 1 % (*v*/v) acetic acid. The chitosan solution was mixed with CF in different ratios (*w*/w) of 1:0.1, 1:0.2, 1:0.5, 1:1, 1:2, 1:5, and 1:10 (with the corresponding CF contents being 9.09 %, 16.67 %, 33.33 %, 50.00 %, 66.67 %, 83.33 %, and 90.90 %, respectively, based on the total composite weight) to cast films for molecular and mechanical characterization (Table S5). For the preparation of chitosan/carbon fiber/silk fibroin (CsCF/SF) film, the SF powder (3.23 %, 6.25 %, and 14.29 % (*w*/w) based on composite mass) was added to the chitosan/carbon fiber (CsCF) mixture (with 66.67 % CF loading) as prepared above and well mixed with a spatula followed by casting. The samples were referred to as CsCF/$SF_{0.1}$, CsCF/SF, and CsCF/$SF_{0.5}$, respectively. For the preparation of the chitosan, CsCF, and CsCF/SF 3D printing inks, first, a certain amount of chitosan was dispersed in DI water, then 15 vol% of acetic acid was added with vigorous hand mixing, and the resulting chitosan gel was kept at room temperature for 7 days to ensure complete solubility. CF powder (66.67 % (w/w) based on the chitosan mass) was then mixed into the chitosan gel well with a spatula, followed by the addition of 6.25 % SF powder (based on the composite mass) and composite inks were well mixed until a smooth paste was obtained.

2.4. Characterization of chitosan/carbon fiber composites

2.4.1. Fourier transform infrared spectroscopy (FT-IR)

The infrared spectra of the composite materials were recorded on a FT-IR spectrophotometer (Cary 630 FTIR spectrometer, Agilent Technologies, USA) with a resolution of 4 cm^{-1} and an accumulation of 32 scans in the range of 4000 to 650 cm^{-1} on an ATR mode. The degree of deacetylation (DD) of chitosan was estimated from the ratio of the FTIR absorption peak at 1648 cm^{-1} (intensity corresponding to the DD) and 1648 cm^{-1} (intensity independent of the DD) using Eq. (2) below (Khan, Kok-Khiang, & Ch'ng, 2002) (Fig. S4):

$$DD(\%) = 100 - \left(\frac{A_{1648}}{A_{3280}} \times 115\right) \tag{2}$$

2.4.2. Nuclear magnetic resonance (NMR) spectroscopy

High-resolution ^{13}C solid-state cross-polarization/magic-angle sample-spinning NMR (^{13}C CP/MAS NMR) measurements of chitin samples were recorded on a Bruker Avance III 850 MHz spectrometer at 20 °C. The powdered samples were placed in a 4 mm zirconia rotor, and spectra were recorded using cross-polarization magic-angle spinning at 10 kHz. The ^{13}C NMR spectrum was referenced against the carboxylate resonance at 177.8 ppm of the standard L-alanine spectrum.

2.4.3. Scanning electron microscopy (SEM)

The surface morphology and fibrous structures of the composite films were examined using a field-emission scanning electron microscope (FESEM) (Zeiss Sigma field emission gun microscope Carl Zeiss AG, Oberkochen, Germany) at an accelerating voltage of 5 kV. Dried films were bonded to carbon tape on aluminum stubs and sputter-coated with gold for 30 s.

2.4.4. Tensile mechanical analysis

The tensile properties of the composite materials were measured on a Shimadzu (AG-X) universal testing machine equipped with a 1 kN load cell according to the standard method (ASTM D3039) with minor modifications (De Baere, Van Paepegem, Quaresimin, & Degrieck, 2011). Acrylic sheets were laser-cut, and specimens were cast into them (in 100 mm × 20 mm × 3 mm dimension) with an additional support sheet and dried in a convective oven at 40 °C for 24 h prior to analysis. Each specimen was wrapped with 2–3 layers of paper strip to protect the gripped area, clamped to the grips, and pulled at a rate of 2 mm/min until fracture occurred at ambient conditions (18 °C temperature and 55 % relative humidity). The thickness and width of the films were measured using a digital caliper to calculate the tensile stress (σ, load per unit cross-sectional area, in the unit of MPa) on the sample. The Young's modulus of materials was calculated by fitting the linear curve on the stress vs. strain curve in the initial elastic region and taken as the slope of this linear region.

2.4.5. Water uptake analysis

The water uptake data of the composite films (20 mm × 20 mm × 2 mm) was calculated by soaking the samples for a certain period of time according to Eq. (3):

$$Water\ uptake\ (\%) = \frac{M_w - M_d}{M_d} \times 100 \tag{3}$$

where M_d is the initial weight of the film, and M_w is the weight of the film after water soaking for a certain period of time at 20 °C.

2.4.6. Thermogravimetric analysis (TGA)

Thermogravimetric analysis of the samples was carried out on a PerkinElmer STA-6000 thermal analyzer in the temperature range of 30–800 °C at a heating rate of 10 °C/min under a nitrogen atmosphere.

2.5. Rheological characterization of printing inks

The rheological properties of the chitosan, CsCF, and CsCF/SF samples were characterized using a controlled stress rheometer (Discovery HR-10 Hybrid rheometer, TA Instruments). A 40 mm parallel plate geometry with a gap of 1000 μm was used. The flow behaviors of the composites were analyzed by measuring the steady-shear viscosity and shear stress as a function of shear rate (0.1–200 s^{-1}). The power-law model was fitted to the plot of shear stress vs. shear rate (Eq. (4)):

$$\tau = K\gamma^{n} \tag{4}$$

where K is the consistency coefficient, and n is the flow behavior index.

The thixotropic behavior of the gels was measured using the hysteresis loop method, where the shear rate was applied from 0.1 to 20 s^{-1} in an upward sweep followed by a downward sweep from 20 to 0.1 s^{-1} for 60 s in each step. The area under the upward curve (A_{up}) and downward curve (A_{down}) was obtained, and thixotropic area A_r was calculated using Eq. (5) (Sanandiya, Vasudevan, Das, Lim, & Fernandez, 2019):

$$A_r = \frac{\left(A_{up} - A_{down}\right)}{A_{up}} \times 100 \tag{5}$$

The time-dependent thixotropy was determined by measuring the viscosity as a function of three different step shear rates (1 s^{-1}, 100 s^{-1}, and 1 s^{-1}) for 60 s in each step.

An oscillatory strain sweep (0.1–100 % strain) at an angular frequency of 1 Hz was performed to obtain the viscoelastic region, followed

by an oscillatory amplitude sweep in the range of 0.1–2000 Pa stress at a frequency of 1 Hz to measure the storage (G') and loss moduli (G'').

2.6. 3D printing

CsCF and CsCF/SF meshes were printed on a commercially available multi-purpose 3D printer with a three-axis motion system (Axo A3, Axolotl Systems, Turkey) equipped with an external air compressor. Fluid extrusion was carried out using a pneumatic fluid dispensing system, with disposable 3 CC luer-tipped syringes attached to the 3D printer with a pneumatic tool head. All inks were extruded with a 20-gauge tapered tip (Adhesive Dispensing UK, with an inner diameter of 0.66 mm, an outer diameter of 0.91 mm, and a length of 38.1 mm). The G-code to fabricate each sample part was automatically generated from CAD designs using the open-source software Slic3r v1.3.0. The generated G-codes were further manipulated and stimulated on NC Viewer (www.ncviewer.com) to make it compatible with the printer following standard G-code processing protocol. The layering in the X- and Y-directions was calculated by Slic3r with a filament diameter of 0.4 mm. Layering in the *Z*-direction was set manually according to the ink properties. For bases that require full-area filling (at least two layers), a perimeter line was printed first, followed by a perpendicular infill with an overlap to ensure fusion between the perimeter and infill.

2.7. Electrical conductivity analysis

The surface electrical conductivity of the fabricated CsCf and CsCf/SF films (thickness < 1 mm) was measured at ambient conditions using the standard four-probe method on a Jandel multi-purpose four-point probe system equipped with a Jandel RM3000+ test unit (Jandel Engineering Limited, UK). The sheet resistance (R_s) of each sample was measured by applying a current of 10 mA. The conductivity (σ) of the samples was calculated using Eq. (6):

$$Conductivity\ (\sigma) = \frac{1}{R_s \times t} \tag{6}$$

where R_s is the sheet resistance obtained from the equipment, and t is the thickness of the film.

2.8. EMI-shielding performance analysis

The EM attenuation performance of the fabricated nanocomposites was elucidated using a vector network analyzer (VNA) (Model No: ZVL13, R&S) connected to a Keycom waveguide operating in the X-band region (8.2 to 12.4 GHz). The scattering parameters (S_{11}, S_{21}, and S_{12}) of the samples were recorded in this frequency range, and the total EMI-shielding effectiveness (EMI SE) was calculated using the standard equation Eq. (7) as given below (Pai et al., 2020):

$$SE_{Total}\ (\mathrm{dB}) = SE_A + SE_R + SE_{MR} \tag{7}$$

Generally, if SE_A is above 10 dB, the SE_{MR} component can be neglected, and the SE_{Total} is reduced to the sum of only SE_A and SE_R values. The shielding effectiveness SE_{Total}, SE_A, and SE_R can be calculated using the scattering parameters using the following equations Eqs. (8)–(10):

$$SE_{Total}(\mathrm{dB}) = 10log\frac{1}{|S_{21}|^2} = 10log\frac{1}{|S_{12}|^2} \tag{8}$$

$$SE_A(dB) = 10log_{10}\left[\frac{(1-S_{11})^2}{S_{12}{}^2}\right] \tag{9}$$

$$SE_R(dB) = 10log_{10}\left[\frac{1}{(1-S_{11})^2}\right] \tag{10}$$

2.9. Fabrication of strain sensors via freeform 3D printing

The 3D printing toolpath to print a strain sensor was set by manually generating a G-code. The strain sensor was printed following a liquid-in-liquid 3D printing (freeform 3D printing) approach, where a highly stretchable support matrix was prepared with SORTA-Clear™ 12 (Smooth-On Inc., USA). Equal weights of Part A and Part B components of SORTA-Clear™ 12 were mixed in a conical tube followed by centrifugation at 4000 rpm for 5 min to remove entrapped bubbles from the matrix material. The CsCF and CsCF/SF conductive inks were transferred to a 3CC syringe and 3D-printed in a Petri dish containing the

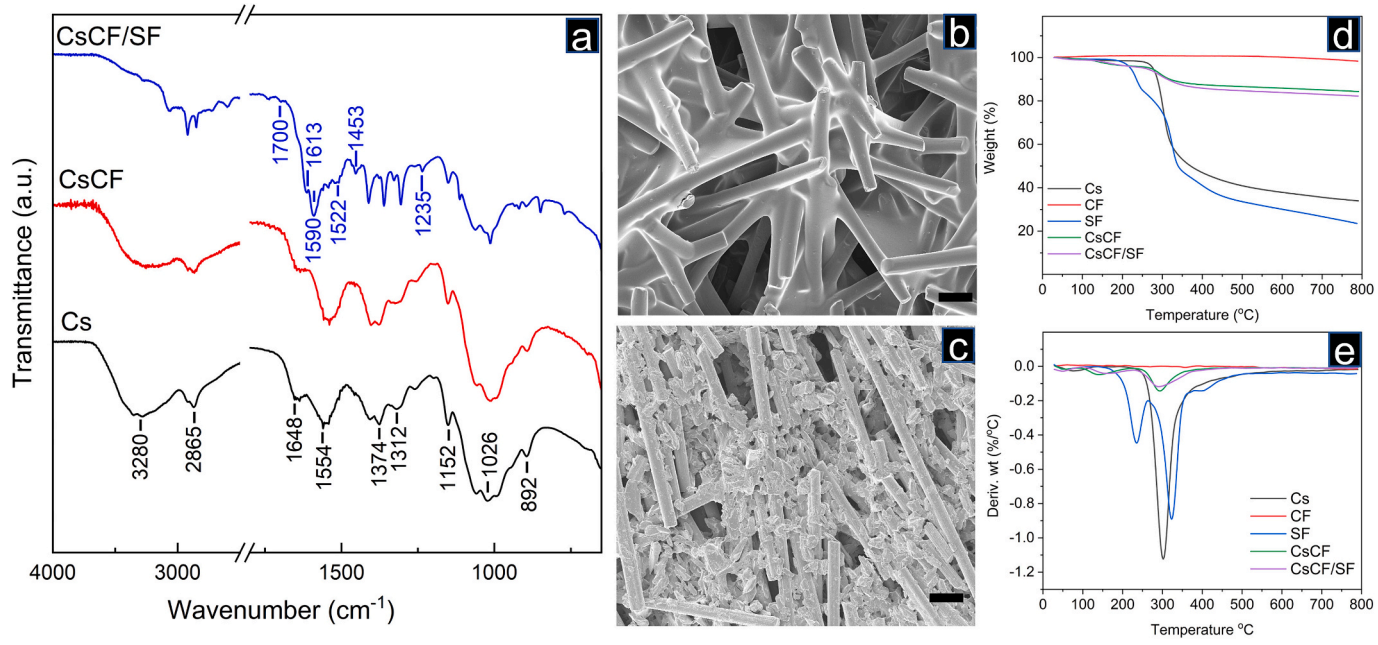

Fig. 1. Characterization of the 10 % (*w/v*) chitosan film (Cs) prepared in 10 % aqueous acetic acid, the chitosan/carbon fiber (CsCF) film with 66.67 % carbon fiber loading, and the CsCF film with 6.25 % silk fibroin loading (CsCs/SF): (a) FTIR spectra for Cs, CsCF, and CsCF/SF; (b, c) SEM images of CsCF and CsCF/SF (scale bar: 20 μm); (d) TGA and (e) DTG curves for Cs, CF, SF, CsCF, and CsCF/SF.

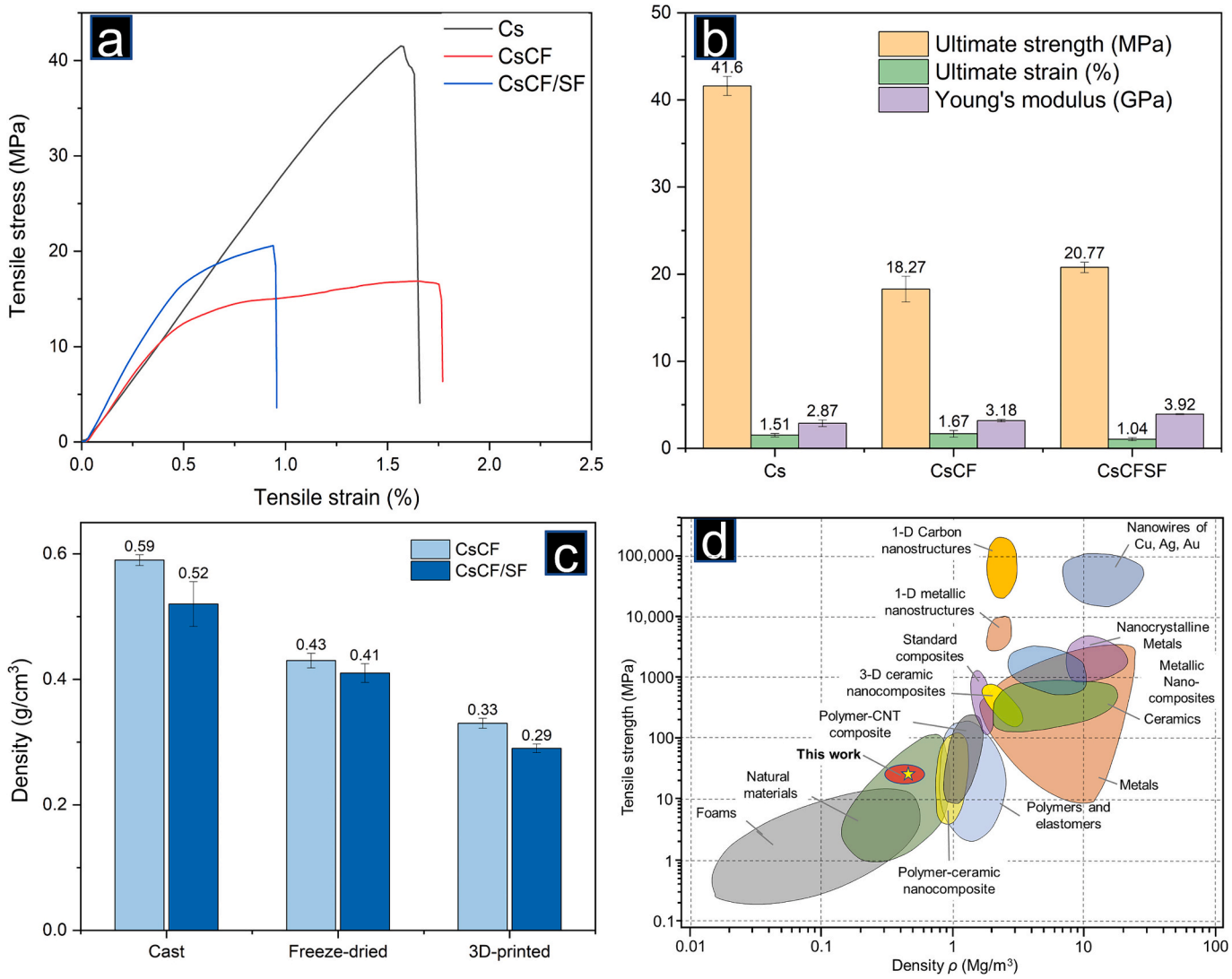

Fig. 2. Mechanical and structural characterization of the 10 % (*w/v*) chitosan (Cs) film prepared in 10 % aqueous acetic acid, the chitosan/carbon fiber film (CsCF) with 66.67 % carbon fiber loading, and the CsCF film with 6.25 % silk fibroin loading (CsCs/SF): (a) Representative tensile stress-strain curves for the Cs, CsCF and CsCF/SF films; (b) tensile strength, strain, and Young's modulus values of the Cs, CsCF, and CsCF/SF films; (c) material density values of the cast, freeze-dried, and 3D-printed CsCF and CsCF/SF composite samples; (d) Ashby plot showing the tensile strength with respect to the density of materials commonly used in polymers and conductive composites; (d) is redrawn from Ref. Ashby, Ferreira, and Schodek (2009) with permission from Elsevier, Copyright 2009.

matrix material at a layer height of 1.5 mm at the print speed of 2.5 mm s^{-1}.

All the experiments conducted for the human body motion test using the strain sensors were carried out in accordance with Newcastle University's guidelines on research involving human participants, which are based on those established by the NHS Health Research Authority (HRA)'s Research Ethics Service, the Declaration of Helsinki, and the Human Rights Act (1998). The University Research Ethics Committee (UREC) at Newcastle University approved the experiments. Informed consent was obtained for experimentation with human subjects.

3. Results and discussion

The first challenge in developing biopolymer-based conductive inks for DIW 3D printing is to modulate the flow, self-supporting, and shape-retention behavior. The 3D printing of biopolymer-based structures is particularly challenging as aqueous media are required to facilitate material flow, while the structures formed by the aqueous inks can maintain their shape without collapsing or shrinking upon drying and exhibit excellent mechanical properties. While aqueous chitosan solutions exhibit favorable adhesive properties, they usually undergo dramatic shrinkage upon drying. Therefore, in this work, we used CF as an active and cost-effective electroconductive substance and found it can also act as a filler to yield a coherent fiber network with chitosan even after drying. It is known that amine group of chitosan form weak interaction with the β-sheet structure of the silk fibroin which facilitate more robust and cohesive network in the hydrogel. This stable network structure is crucial in shape retention after the extrusion through nozzle during 3D printing process. We also found that the shrinkage behavior of chitosan in the composite was further reduced by the addition of SF (protein) due to the interaction between the chitosan and the β-sheet of the SF (Falini, Weiner, & Addadi, 2003) followed by stable network formation. However, a high chitosan concentration increased the risk of generating air pockets in the matrix, especially when samples were cast in a narrow-confined mold for characterization. Therefore, to obtain uniform and smooth films for the molecular and mechanical characterization, a slightly lower concentration of chitosan (10 % *w/v*) in acetic acid (10 % w/v) was used to prevent bubble formation. For 3D printing, 15 % (*w/v*) chitosan in acetic acid (15 % w/v) was used to minimize water content in the ink. The higher concentration of chitosan

did not negatively affect 3D printing because tiny bubbles trapped in the printing ink could diffuse easily during the extrusion due to the formation of thin filaments, unlike in mold casting, where bubbles could not escape, and their accumulation leads to big air pockets.

3.1. Characterization of chitosan-based materials and composites

The chitosan film and the CsCF and CsCF/SF composite films were characterized by FTIR spectroscopy. The characteristic IR bands of the chitosan film (Fig. 1a) were as follows: ν_{max} (cm^{-1}) 3280 br (—OH stretching and –NH stretching), 2865 w (C—H stretching), 1648 s (C═O stretching amide I), 1374 w (C—N stretching amide II), 1152 w (C—O anti-symmetric bridge stretching), 1026 s, br (C—O—C stretching vibration), and 892 w (C1—H deformation vibration). The FTIR spectrum of CsCF did not show significant changes, suggesting the absence of functional groups in the CF (Fig. S5), which is as expected. In CsCF/SF, new IR bands (1700, 1590, 1522, and 1234 cm^{-1}) appeared, which can be attributed to different amide bonds in the SF (Table S6 and Fig. S5). For CsCF/SF, the IR bands corresponding to the amide bonds of the SF at 1511, 1443, and 1231 cm^{-1} were slightly shifted to shorter wavelengths and appeared at 1522, 1451, and 1235 cm^{-1}, indicating the molecular level interaction presumably by hydrogen bonds between the SF and the chitosan (Falini et al., 2003).

Fig. 1b and c is the SEM images of CsCF and CsCF/SF, respectively, showing the different components were thoroughly mixed and CF was bonded with the chitosan. The fiber length of the CF imaged by SEM was analyzed using ImageJ software by collecting measurements of 100 individual fibers (Fig. S6a). The size distribution result of the CF shows a mean fiber length of 51.32 ± 29.53 μm, with 84 % of the fibers being 20–80 μm long, whereas the mean diameter was 5.80 ± 0.52 (Fig. S6b). The SEM images of Cs, CsCF, and CsCF/SF exhibited distinctly different surface morphologies. The Cs film showed a smooth and uniform surface, whereas CsCF appeared as randomly arranged fibers held together by a glue-like substance, indicating that the CF was dispersed well in the chitosan matrix. The addition of SF changed the morphology to a great extent from chitosan-coated fibers to cloud-like agglomerates with visible fibers that are partially aligned compared to CsCF.

The thermal stability profiles of the chitosan, CF, and SF powder and their composite films were analyzed using thermogravimetric (TG) and differential thermogravimetric (DTG) analyses, as shown in Fig. 1d and e. The CF showed excellent thermal stability with a negligible mass loss of 1.58 % up to 800 °C, likely due to moisture loss. However, the chitosan exhibited a single mass loss step of approximately 50 % in the temperature range of 250–350 °C, with a subsequent gradual degradation resulting in a residual mass of 34 % on heating up to 800 °C. The SF sample exhibited a two-step mass loss behavior, with the first step occurring between 150 and 250 °C (a mass loss of 18 %) followed by a second step between 260 and 380 °C (a mass loss of 53 %), with a residual mass of 23.43 % after gradual degradation. The CsCF composite film exhibited a similar two-step mass loss behavior, with the first step occurring between 92 and 220 °C (5 % mass loss) and the second between 224 and 430 °C (a 13 % mass loss), with a residual mass of 15.55 % after gradual degradation. The CsCF/SF composite film also exhibited a two-step mass loss pattern, with the first step occurring between 105 and 230 °C (a 4.8 % mass loss) followed by the second step between 230 and 470 °C (a 13 % mass loss); however, the residual mass increased to 17.70 % after gradual degradation. Additionally, the shift in the mass loss temperature of the CsCF (140 °C and 293 °C) and CsCF/SF (159 °C and 291 °C) composite films compared to the pure chitosan (302 °C) and SF (323 and 235 °C) indicates an interaction between chitosan and SF molecules that altered their thermal degradation characteristics.

Table 1
Rheological data for the chitosan (Cs) in 10 % aqueous acetic acid, the chitosan/carbon fiber (CsCF) gel with 66.67 % carbon fiber loading, and the chitosan/carbon fiber gel with 6.25 % silk fibroin loading (CsCs/SF).

	Viscosity (η) (Pa·s) at shear rate		Flow behavior index (n)	Consistency coefficient (K)	R^2	Yield stress (τ_y) (Pa)
	1 s^{-1}	10 s^{-1}				
Cs	58.80	36.52	0.759	50.44	0.9932	32.45
CsCF	255.84	138.51	0.609	210.41	0.9787	172.16
CsCF/SF	178.92	80.80	0.636	143.47	0.9803	103.32

The mechanical and structural properties of the chitosan film and the CsCF and CsCF/SF composite films were examined by measuring their tensile strength, Young's modulus, and density. Initially, the specimens were cast in a dog-bone shape according to the ASTM standard (Fig. S7a). However, during the drying process, the small air bubbles were trapped within the samples, which then accumulated to form bigger air pockets due to the high viscosity of chitosan (Fig. S7c). To overcome this problem, the mold was redesigned to produce long film pieces of 110 × 20 cm, which were tested for tensile strength (Fig. S7d, e, and f). The representative stress-strain curves for each sample and the mechanical property results are shown in Fig. 2a and b. The tensile strength of the chitosan film and the CsCF and CsCF/SF composite films were 41.60 ± 1.09, 18.27 ± 1.46, and 20.77 ± 0.60 MPa, respectively, and their ultimate strains were 1.5 ± 0.20, 1.67 ± 0.38, and 1.04 ± 0.17 %, respectively. The Young's modulus of those are 2.87 ± 0.38, 3.18 ± 0.15, and 3.92 ± 0.06 GPa, respectively (Fig. S8). The result showed that the addition of CF to the chitosan significantly reduced the tensile strength, which is expected due to the hydrophobic effect of the CF on the chitosan. The presence of SF in the CsCF composite slightly increased the tensile strength and Young's modulus, presumably due to the partial alignment of the CF (see the SEM image in Fig. 1c), as well as the interaction between chitosan and SF (see the FTIR result in Fig. 1a).

The densities of the CsCF and CsCF/SF composite films prepared by different fabrication methods (casting, freeze drying, and 3D printing) are shown in Fig. 2c. Here, these three distinct approaches were used to fabricate composite with tailored material characteristics (e.g., surface area and density) and manufacturability (e.g., pliability and viscoelastic properties). The casting process can demonstrate the fabrication of thin and compact sheets, and freeze-drying produces lightweight porous foams, whereas 3D printing can accomplish personalized density and complex shapes based on their intended applications. For CsCF, the highest density was observed for the cast sample (0.59 ± 0.009 g/cm^3), followed by the freeze-dried one (0.43 ± 0.012 g/cm^3), and the 3D-printed one (0.33 ± 0.008 g/cm^3). A similar pattern was observed for the CsCF/SF composite samples prepared by solution-casting (density 0.52 ± 0.036 g/cm^3), freeze-drying (density 0.41 ± 0.015 g/cm^3), and 3D-printing (density 0.29 ± 0.007 g/cm^3). The relatively high density of the cast samples could be due to the shrinking nature of chitosan, which could pull the fibers together and result in a tightly packed arrangement. Nevertheless, freeze-drying could generate voids when water molecules sublimate, resulting in lower density of the freeze-dried samples. The density of CsCF/SF decreased further to 0.35 ± 0.02 g/cm^3 when the samples underwent supercritical drying with liquid carbon dioxide as the super critical fluid. In the 3D-printed films, the infill was set to 22.5 % to produce low-density grids.

As shown in Fig. 2d, the series of composites developed here with the chitosan, CF, and SF possessed mid-range density with high ultimate tensile strength in the natural material category. Considering the low density of the composite, the approximate material cost is <20 USD/kg, which can produce a 5 m × 5 m square 3D-printed panel with 1 mm thickness.

The water uptake capacity of the CsCF and CsCF/SF composite films was measured by calculating the mass of water retained by the composites after water immersion. After 2 h, both composites showed to be saturated, uptaking ~54 and ~ 44 % water, respectively, at 20 °C (Fig. S9).

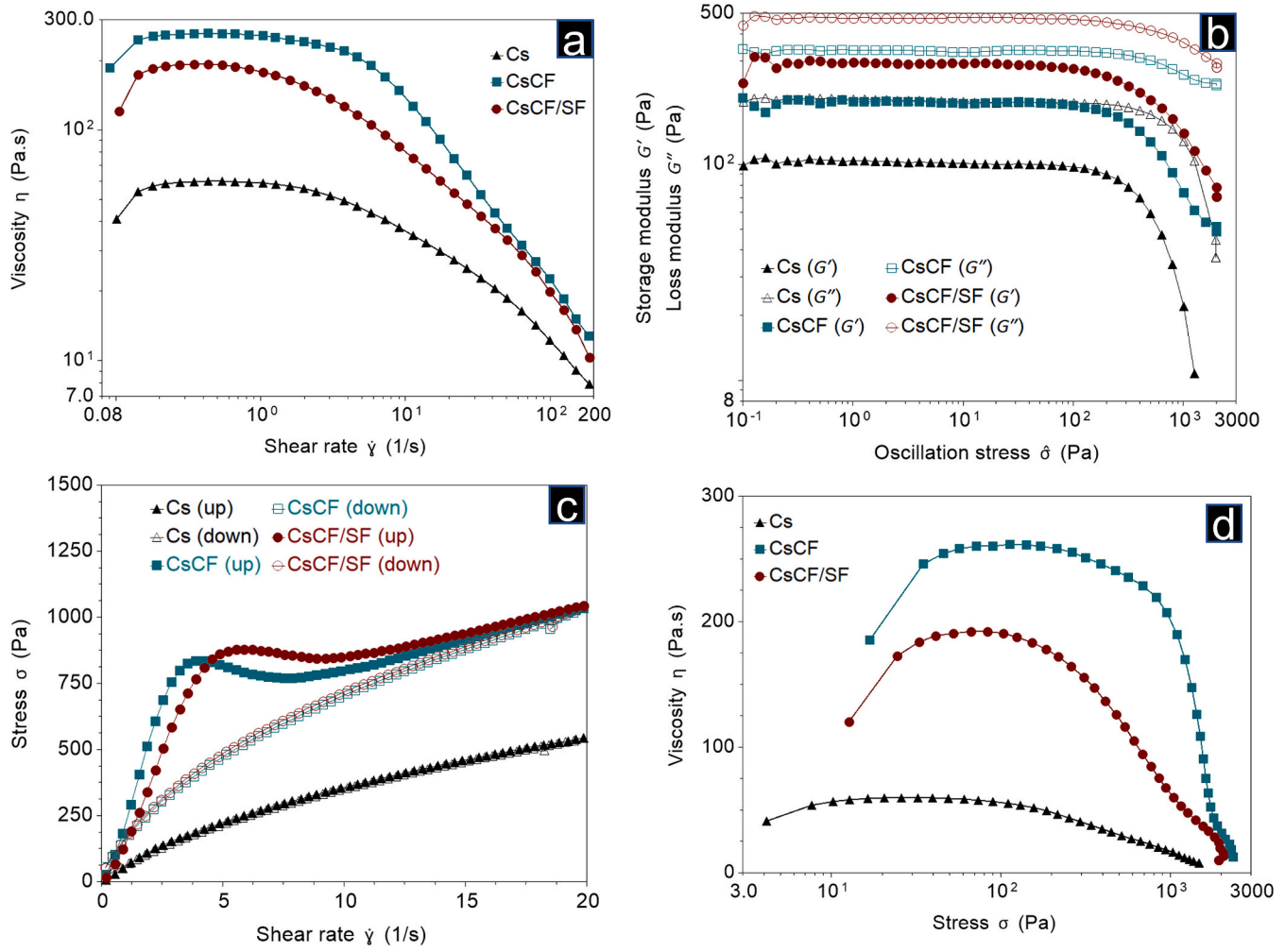

Fig. 3. Rheological characteristics of the 10 % (*w/v*) chitosan gel (Cs) prepared in 10 % aqueous acetic acid, the chitosan/carbon fiber (CsCF) gel with 66.67 % carbon fiber loading, and the chitosan/carbon fiber gel with 6.25 % silk fibroin loading (CsCs/SF): (a) Viscosity (η) as a function of shear rate; (b) storage modulus (G') and loss modulus (G'') as a function of oscillatory stress; (c) thixotropic hysteresis loop by measuring shear stress as a function of increasing shear rate (the upward curve) and decreasing shear rate (the downward curves); (d) yield stress determination by measuring viscosity as a function of shear stress.

3.2. Rheological characteristics

Rheological studies are critical for determining the printability of inks for pneumatic-based printing (Xie, 2023). An ink that is shear-thinning, meaning it has a low viscosity at high shear rates, is ideal for extrusion from the nozzle. In this context, the dynamic viscosities (η) of the chitosan, CsCF, and CsCF/SF inks as a function of shear rate were examined. The η values of the Cs, CsCF, and CsCF/SF inks at a low shear rate (1 s^{-1}) were 58.80, 255.84, and 178.92 Pa·s, respectively, which significantly decreased at a higher shear rate (10 s^{-1}) to 36.52, 138.51, and 80.80 Pa·s, respectively (see Table 1 and Fig. 3a). The shear rate vs. shear stress curves were fitted with power law approximation to obtain flow behavior index (n) and consistency coefficient (K) values. All three samples had $n < 1$, which confirms their shear-thinning behavior. The inks exhibited a low viscosity at moderate shear rates (~10 s^{-1}), such as during an extrusion process.

The flow curves were also fitted to different fluid models, and the best fit of the statistical data (with the maximum R^2 value given) to the Herschel-Bulkley model indicates a non-Newtonian fluid with yield stress (τ_y) (Table 1). Yield stress is the stress beyond which the strength of the gel network is compromised, and the material starts to flow. It is considered the most important factor for high printability and shape fidelity (Xie, 2023). The τ_y values of the chitosan, CsCF, and CsCF/SF inks were 32.45, 172.16, and 103.32 Pa, respectively (Fig. 3d). For DIW 3D printing, an τ_y value of >100 Pa is adequate; therefore, both the CsCF and CsCF/SF inks have enough τ_y for 3D printing.

The thixotropic behavior of the materials was evaluated by performing a hysteresis loop test to calculate the inbound area between the upward and downward curves, which can indicate the stress-dependent deformation and regeneration of the microstructure in a material. The thixotropic area (A_r) of the chitosan, CsCF, and CsCF/SF inks were 4.74 %, 16.11 %, and 16.52 %, respectively (Fig. 3c). The time-dependent thixotropy was also carried out using oscillatory mode to examine the rate of structural breakdown and recovery in the material (Fig. S10), which shows time-dependent changes in the viscosity of the ink before, during, and after the extrusion. The total thixotropy times of the samples were calculated by the time differences between the end of the second step (structural deformation phase) and the time in the third step when the maximum viscosity was achieved (structural regeneration phase). The structure recovery of the chitosan, CsCF, and CsCF/SF inks were 96.48 %, 92.75 %, and 94.59 %, respectively, whereas the total thixotropy times were 2 s, 36.22 s, and 34.14 s, respectively.

Dynamic (oscillatory) rheological tests were also carried out to determine G'' and G' values. Fig. 3b illustrates that the Cs, CsCF, and CsCF/SF inks all demonstrated G'' values higher than G', indicating their liquid-like characteristics, suitable for use as flowable inks.

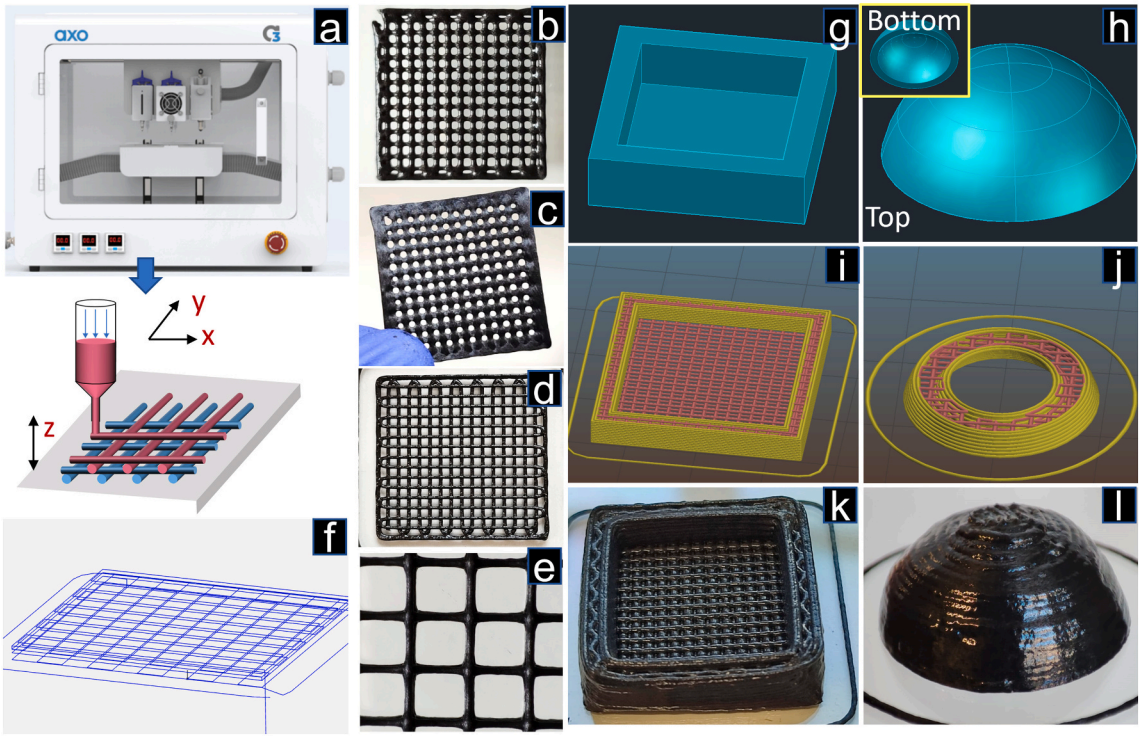

Fig. 4. 3D printing setup: (a) DIW-type bioprinter with pneumatically driven extrusion via an external air compressor and variable printheads used in this study. 3D printing of a chitosan/carbon fiber (CsCF) ink prepared with a 15 % chitosan paste and 66.67 % carbon fiber loading and of the CsCF gel with 6.25 % silk fibroin loading (CsCs/SF): (b, c) 3D-printed CsCF grid before and after drying in an oven at 40 °C for 12 h; (d, e) 3D-printed CsCF/SF grid before and after drying in an oven at 40 °C; (f) representative toolpath generated by G-codes to 3D print grids; CAD designs of (g) a rectangular shell and (h) a dome-shape shell commonly used in circuit board (PCB); 3D layers detail of (i) the rectangular-shape shell and (j) the dome-shape shell; (k) the 3D-printed dome-shape shell; (l) the 3D-printed rectangular-shape shell.

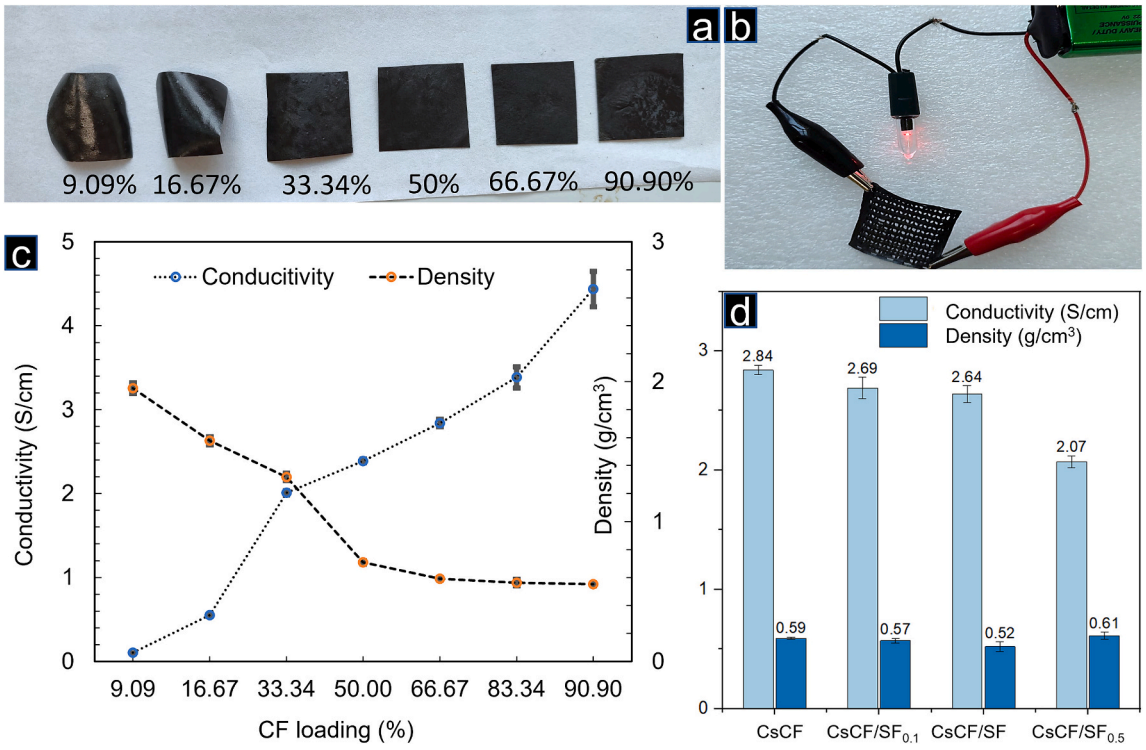

Fig. 5. Electrical conductivity of the chitosan/carbon fiber (CsCF) gel prepared with a 10 % chitosan gel and 66.67 % carbon fiber loading: (a) Photograph of the CsCF/SF composite films with different carbon fiber loadings; (b) visual demonstration of the electroconductivity of the 3D-printed chitosan/carbon fiber/silk fibroin (CsCF/SF) grid using a 9 V battery as a DC power source; (c) graph of conductivity and density as a function of carbon fiber (CF) content; (d) density of the CsCF composite film and the CsCF/SF films with different silk fibroin loadings (3.23 %, 6.25 %, and 14.28 % for CsCF/$SF_{0.1}$, CsCF/SF and CsCF/$SF_{0.5}$, respectively).

3.3. Optimization of 3D printing

The 3D printability of the chitosan/CF ink was optimized by evaluating the effect of CF loading on the ability of the ink to reach a suitable viscosity and retain the shape. As the composite ink consisted of an aqueous solution of chitosan, it was preferred to print with a minimum amount of water (i.e., high chitosan concentration) to achieve high print fidelity and shape retention of the 3D printed structures. The highest possible concentration of chitosan that can be reached for the 3D printing of single-layer grids was 15 % (w/v) in 15 % acetic acid (with the 3D printer and a schematic illustration of line printing shown in Fig. 4a). However, it was found that 3D-printed grids shrank vertically during the drying process, the printed grid lines were flattened into a ribbon shape, and the crossover point of vertical and horizontal grid lines fused (Fig. 4b, and c). Interestingly, the incorporation of 20 % SF effectively eliminated the shrinkage effect, and the 3D-printed lines in the grids were observed to be cylindrical and retain their shape even after drying (Fig. 4d and e). To produce 3D-printed multilayer grids, the G-codes were manipulated in such a fashion that the toolpath of every 2 subsequent layers offset to the center of two lines of previous layers to produce 3D inter-woven grids (Video S3). To demonstrate the printability of the CsCF/SF ink for complex geometries, we mimicked the printing of an EMI-shielding rectangular shell with 20 consecutive layers, a common component in printed circuit boards (PCB) (Fig. 4g, i, and k; Video S1) and a spherical dome with a cavity underneath (Fig. 4h, j, and l; Video S2). Printing the rectangular shell demonstrates the material's ability to withstand the multiple layers without losing its confined shape, while the 3D printing of the hollow dome demonstrates the material's ability to print overhanging structures for certain geometries. Chitosan composites have been reported as sustainable composites to produce large-scale structures up to 5 m in height using an industrial robot (Dritsas et al., 2018) and are a promising candidate for building artificial ecosystems for terraforming Mars (Shiwei, Dritsas, & Fernandez, 2020). Due to their numerous benefits, such as 3D printability, lightweight, conductivity, and cost-effectiveness, the CsCF and CsCF/SF composites developed in this study may be compelling materials to further investigate for extraterrestrial manufacturing and space exploration.

3.4. Electrical conductivity and EMI shielding performance

The EMI shielding effectiveness of a material is highly dependent on its electrical conductivity. In order to evaluate the conductivity of the material in relation to the carbon loading, the sheet resistance of thin films was measured following the van der Pauw method using four-probe to avoid interference from the contact resistance, and conductivity was calculated using Eq. (6) (Fig. 5a and b). The CF is an active conductive ingredient in the developed ink, which was optimized for maximized conductivity and optimum printability. Fig. 5c shows the conductivity of the chitosan/CF composites with different carbon loadings (0–90.90 %). The conductivity of the composites was directly proportional to the CF loading. The lowest CF loading in the CsCF composite to achieve conductivity (0.10 S/cm) was 9.09 %. The CsCF ink optimized for the highest printing fidelity with a CF loading of 66.67 % showed a conductivity of 2.83 S/cm. Conductivity increased further (4.23 s/cm) with a higher carbon loading (90.90 %), although the material lost its pliability for 3D printing due to high viscosity. The optimized carbon fiber loading (66.67 %) was further used to evaluate the effect of SF addition on conductivity. The addition of the silk fibroin slightly reduced the conductivity, as shown in Fig. 5d. The addition of 3.23 %, 6.25 %, and 14.29 % SF (i.e., CsCF/$SF_{0.1}$, CsCF/SF, and CsCF/$SF_{0.5}$, respectively) decreased the conductivity by 5.28 %, 7.04 %, and 27.11 %, respectively. The addition of 6.25 % SF did not decrease conductivity significantly; rather, it improved the printing fidelity and shrinking behavior. Therefore, the optimized CsCF/SF composite with 6.66 % SF loading was further used to evaluate the EMI-shielding

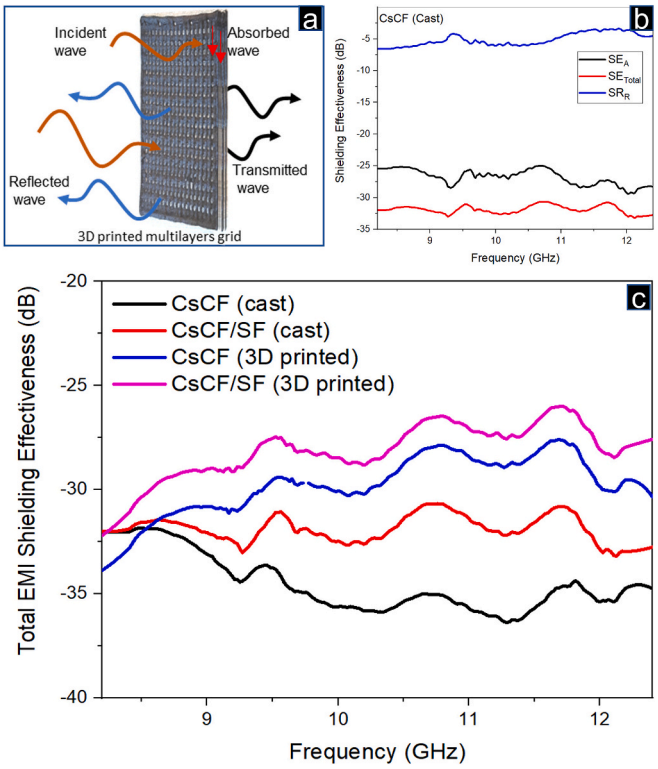

Fig. 6. (a) schematic illustration of the 3D printed multilayer grid; (b) EMI-shielding effectiveness (SE_{total}, SE_A, and SE_R) of the cast chitosan/carbon fiber (CsCF) composite (with 66.67 % CF loading) film as a representative graph; (c) comparison of SE_{total} between the CsCF composite samples and the chitosan/carbon fiber/silk fibroin (CsCF/SF) composite (with 66.67 % CF and 6.25 % SF loading) samples fabricated by either casting or 3D printing.

effectiveness. The decline in electrical conductivity of the CsCF/SF composite as the SF content increased can be attributed to the non-conductive nature of SF, leading to a higher proportion of non-conductive materials in the composite. Furthermore, the reduced shrinkage of the CsCF/SF composite, attributed to the interaction between chitosan and SF, resulted in the formation of a stronger network that allowed for increased spacing between CF compared to the CsCF composite.

The principle of EMI shielding relies on the use of conductive or magnetic materials to reflect, transmit, and absorb electromagnetic radiation (Fig. 6a). The EMI-shielding performance of the material is evaluated by shielding effectiveness (SE), which is determined by the ratio of incident and transmitted energies (SE_A and SE_R) of EM radiation at a given frequency. The EMI-shielding effectiveness of the composite films was determined in the X-band frequency, which is used by satellite communications, weather monitoring, defense tracking, and air traffic control systems. The formation of a highly interconnected network of conductive CF plays a crucial role in influencing the overall EMI-shielding performance. Fig. 6b shows the representative plots for the EMI-shielding effectiveness (SE_{total}, SE_A, and SE_R) of the cast CsCF film, and Fig. 6c shows a comparison of the total SE value between the CsCF and CsCF/SF composite samples fabricated by casting and 3D printing. The maximum EMI SE value of 32–35 dB was observed for the cast CsCF film with a thickness of 1 mm. This can be attributed to the higher conductivity (2.84 ± 0.04 S/cm) of this sample compared to the others. Moreover, all five samples with different formulations and fabrication processes exhibited total EMI-shielding effectiveness in the range of 26–36 dB and showed higher SE_A values than SE_R values, indicating an absorption-dominant EMI-shielding behavior of these composites (Figs. S11–12). The high total SE values (SE_t) indicate very good (where $SE_t < 30$ dB) to excellent (where $SE_t > 30$ dB) shielding performance by

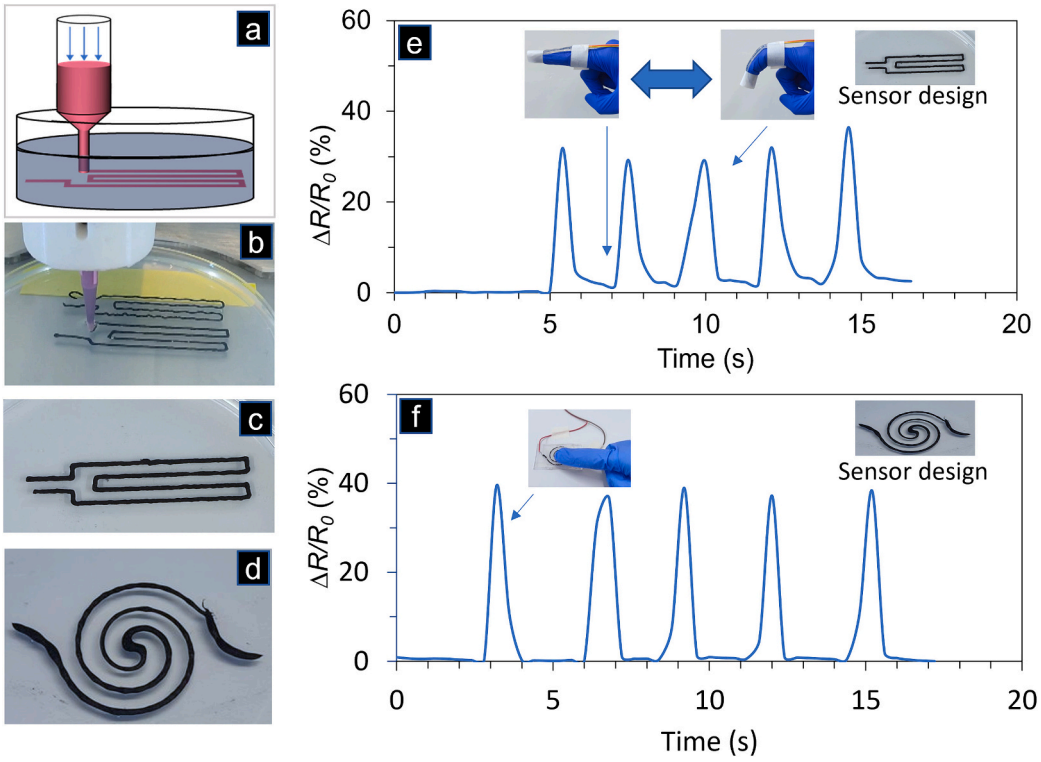

Fig. 7. Freeform 3D printing of a strain sensor using the chitosan/carbon fiber/silk fibroin (CsCF/SF, with 66.67 % carbon fiber and 6.25 % silk fibroin loading) ink via liquid-in-liquid extrusion process: (a) Illustration of liquid-in-liquid extrusion; (b) 3D printing of the CsCF/SF ink into a liquid support bath of the SORTA Clear™ 12 silicone elastomer; printed (c) linear and (d) spiral sensors in the silicone elastomer support bath after curing; (d) strain sensing experiment by bending the finger to record changes in resistance using linear sensor; (f) strain sensing experiment by pressing the spiral sensor to changes in the resistance.

blocking 99.0–99.9 % incident electromagnetic waves, respectively, in all composites (Mishra, Thomas, Abraham, Joseph, & Thomas, 2018). This is very important as the secondary reflections are minimized, and more incident EM energy is absorbed and dissipated as heat.

3.5. *Freeform 3D printing of strain sensors*

The developed inks were further investigated for their printability in a silicone elastomer support bath using a liquid-in-liquid extrusion (freeform additive manufacturing) approach (Fig. 7a; Video S4). The pre-cured translucent viscous liquid used as a support bath can achieve excellent tensile strength after curing, making it an ideal substrate for freeform 3D printing of sensors. The CsCF and CsCF/SF inks were printed into the silicone matrix and then cured for 12 h at 20 °C to realize an encapsulated conductive ink embedded in a stretchable polymeric matrix (Fig. 7b, and c). The CsCF ink formed spherical droplets after printing due to the highly hydrophobic nature of the silicone polymer (Fig. S13). However, the addition of SF altered the interaction with the silicon substrate and improved its printability. The resulting strain sensor was connected to metal wires, and a strain-sensing experiment was conducted by bending the sensor on a finger at angles ranging from 0 to 45° to measure changes in resistance (Fig. 7e). The strain sensor was capable of detecting the bending movement of the finger by changing its resistance, demonstrating the potential of the biobased CsCF/SF conductive ink in wearable sensing devices. Moreover, a sensor with a spiral design was fabricated for compressive sensing (Fig. 7d and f). While both sensors exhibited similar sensitivity in terms of relative resistance change ($\Delta R/R_0$), the linear sensor exhibited greater $\Delta R/R_0$ during bending test, whereas the spiral sensor showed more significant $\Delta R/R_0$ during compression experiments.

4. Conclusion

Based on chitosan as a binder, CF as a low-cost electroconductive filler, and a small amount of SF (6.25 %) as a structural stabilizer, lightweight, cost-effective, versatile 3D-printing inks were developed. The CsCF and CsCF/SF inks showed shear-thinning behavior with a structural recovery of ~92–94 % within a duration of 34–36 s. The inks exhibited excellent post-printing structure retention. The developed ink did not require additional crosslinking or curing treatment during printing or post-printing. FTIR and TGA indicated the interaction between chitosan chains and the amide groups of the β-sheet of SF, similar to those found in nature where specific load-bearing properties are required, while SEM analysis revealed an interconnected network of fibers in the composites. The structural density of the cast CsCF and CsCF/SF composites was 0.59 ± 0.009 and 0.52 ± 0.036 g/cm^3, respectively, while that of the 3D-printed grids was 0.33 ± 0.008 and 0.29 ± 0.007 g/cm^3, respectively. The freeze-dried CsCF and CsCF/SF foam showed densities of 0.43 ± 0.012 and 0.41 ± 0.015 g/cm^3, respectively. The range of density vs. conductivity obtained by different fabrication processes demonstrates their capabilities to achieve customized density for desired applications. The electroconductivity of CsCF and CsCF/SF were 2.84 ± 0.043 and 2.64 ± 0.065, respectively. The incorporation of SF into the CsCF composite at a moderate level (6.25 %) did not significantly alter the electrical and rheological properties but greatly improved the printing accuracy and stability and slightly increased the tensile strength and density. The EMI-shielding effectiveness of the cast CsCF and CsCF/SF films was 32–36 dB and 32–33 dB, respectively, while for the 3D printed composites, it was 28–34 dB and 30–31 dB, respectively, which indicates very good (where $SE_t < 30$ dB) to excellent (where $SE_t > 30$ dB) shielding performance by blocking >99.0 % incident electromagnetic waves in all composites. Moreover, freeform 3D printing of linear and spiral strain sensors using the CsCF/SF composite ink was demonstrated, and the sensors showed

commendable sensitivity of $\Delta R/R_0$ to finger bending and compression, respectively.

The composite inks developed in this study can be formulated by simple mixing of different components without organic solvents or chemical reactions. Considering their low density, high conductivity, and easy manufacturability, the presented biopolymer-based composites have the potential to be developed as conductive foams or customized 3D structures on a small as well as large scale for the electronics and aerospace industry.

The supplementary data consists of Figs. S1 to S13 and Tables S1 to S6 contained in a PDF file and Video clips S1 to S4 demonstrating the 3D printing of rectangular shells, spherical hollow domes, 3D multilayers grids, and strain sensors, respectively. Supplementary data to this article can be found online at https://doi.org/10.1016/j.carbpol.2024.122161.

CRediT authorship contribution statement

Naresh D. Sanandiya: Writing – original draft, Visualization, Validation, Software, Methodology, Investigation, Formal analysis, Data curation, Conceptualization. **Avinash R. Pai:** Writing – original draft, Investigation. **Shayan Seyedin:** Resources, Methodology, Investigation. **Fengzai Tang:** Investigation. **Sabu Thomas:** Resources. **Fengwei Xie:** Writing – review & editing, Writing – original draft, Supervision, Resources, Project administration, Methodology, Funding acquisition, Conceptualization.

Declaration of competing interest

The authors declare the following financial interests/personal relationships which may be considered as potential competing interests: Fengwei Xie reports financial support was provided by Engineering and Physical Sciences Research Council.

Data availability

The data of this work are available at https://doi.org/10.25405/data.ncl.23284328

Acknowledgments

This research was financially supported by the Engineering and Physical Sciences Research Council (EPSRC) [grant number EP/V002236/2]. Authors also acknowledges funding from the Royal Society via a Research Grant (RGS\R2\222071). The UK High-Field Solid-State NMR Facility used in this research was funded by EPSRC and BBSRC (EP/T015063/1) as well as the University of Warwick, including via part funding through Birmingham Science City Advanced Materials Projects 1 and 2 supported by Advantage West Midlands (AWM) and the European Regional Development Fund (ERDF). The authors acknowledge assistance from the Facility Manager Team Dinu Iuga at the University of Warwick for acquiring NMR data.

References

Ashby, M. F., Ferreira, P. J., & Schodek, D. L. (2009). Chapter 1 - nanomaterials and nanotechnologies: An overview. In M. F. Ashby, P. J. Ferreira, & D. L. Schodek (Eds.), *Nanomaterials, nanotechnologies and design* (pp. 1–16). Boston: Butterworth-Heinemann.

Cernencu, A. I., Lungu, A., Stancu, I.-C., Serafim, A., Heggset, E., Syverud, K., & Iovu, H. (2019). Bioinspired 3D printable pectin-nanocellulose ink formulations. *Carbohydrate Polymers, 220*, 12–21.

De Baere, I., Van Paepegem, W., Quaresimin, M., & Degrieck, J. (2011). On the tension–tension fatigue behaviour of a carbon reinforced thermoplastic part I: Limitations of the ASTM D3039/D3479 standard. *Polymer Testing, 30*(6), 625–632.

Demirtaş, T. T., Irmak, G., & Gümüşderelioğlu, M. (2017). A bioprintable form of chitosan hydrogel for bone tissue engineering. *Biofabrication, 9*(3), Article 035003.

Dritsas, S., Halim, S. E. P., Vijay, Y., Sanandiya, N. G., & Fernandez, J. G. (2018). Digital fabrication with natural composites. *Construction Robotics, 2*(1), 41–51.

Du, G., Mao, A., Yu, J., Hou, J., Zhao, N., Han, J., … Bai, H. (2019). Nacre-mimetic composite with intrinsic self-healing and shape-programming capability. *Nature Communications, 10*(1), 800.

Falini, G., Weiner, S., & Addadi, L. (2003). Chitin-silk fibroin interactions: Relevance to calcium carbonate formation in invertebrates. *Calcified Tissue International, 72*(5), 548–554.

Holland, S., Tuck, C., & Foster, T. (2018). Selective recrystallization of cellulose composite powders and microstructure creation through 3D binder jetting. *Carbohydrate Polymers, 200*, 229–238.

Iglesias-Mejuto, A., & García-González, C. A. (2021). 3D-printed alginate-hydroxyapatite aerogel scaffolds for bone tissue engineering. *Materials Science and Engineering: C, 131*, Article 112525.

Keller, A., Stevens, L., & Wallace, G. G. (2016). 3D printed edible hydrogel electrodes. *MRS Advances, 1*(8), 527–532.

Khan, T., Kok-Khiang, P., & Ch'ng, H. (2002). Reporting degree of deacetylation values of chitosan: The influence of analytical methods. *Journal of Pharmacy & Pharmaceutical Sciences, 5*, 205–212.

Liu, S., Hu, Q., Shen, Z., Krishnan, S., Zhang, H., & Ramalingam, M. (2022). 3D printing of self-standing and vascular supportive multimaterial hydrogel structures for organ engineering. *Biotechnology and Bioengineering, 119*(1), 118–133.

Liu, Z., Chen, H., Zheng, B., Xie, F., & Chen, L. (2020). Understanding the structure and rheological properties of potato starch induced by hot-extrusion 3D printing. *Food Hydrocolloids, 105*, Article 105812.

Madaghiele, M., Marotta, F., Demitri, C., Montagna, F., Maffezzoli, A., & Sannino, A. (2014). Development of semi- and grafted interpenetrating polymer networks based on poly(ethylene glycol) diacrylate and collagen. *Journal of Applied Biomaterials & Functional Materials, 12*(3), 183–192.

Mishra, R. K., Thomas, M. G., Abraham, J., Joseph, K., & Thomas, S. (2018). Electromagnetic interference shielding materials for aerospace application: A state of the art. In *Advanced materials for electromagnetic shielding: Fundamentals, properties, and applications* (pp. 327–365).

Pai, A. R., Binumol, T., Gopakumar, D. A., Pasquini, D., Seantier, B., Kalarikkal, N., & Thomas, S. (2020). Ultra-fast heat dissipating aerogels derived from polyaniline anchored cellulose nanofibers as sustainable microwave absorbers. *Carbohydrate Polymers, 246*, Article 116663.

Pakizeh, M., Moradi, A., & Ghassemi, T. (2021). Chemical extraction and modification of chitin and chitosan from shrimp shells. *European Polymer Journal, 159*, Article 110709.

Sanandiya, N. D., Ottenheim, C., Phua, J. W., Caligiani, A., Dritsas, S., & Fernandez, J. G. (2020). Circular manufacturing of chitinous bio-composites via bioconversion of urban refuse. *Scientific Reports, 10*(1), 4632.

Sanandiya, N. D., Vasudevan, J., Das, R., Lim, C. T., & Fernandez, J. G. (2019). Stimuli-responsive injectable cellulose thixogel for cell encapsulation. *International Journal of Biological Macromolecules, 130*, 1009–1017.

Sanandiya, N. D., Vijay, Y., Dimopoulou, M., Dritsas, S., & Fernandez, J. G. (2018). Large-scale additive manufacturing with bioinspired cellulosic materials. *Scientific Reports, 8*(1), 8642.

Shiwei, N., Dritsas, S., & Fernandez, J. G. (2020). Martian biolith: A bioinspired regolith composite for closed-loop extraterrestrial manufacturing. *PLoS One, 15*(9), Article e0238606.

Stein, N., Saathoff, T., Antoni, S.-T., & Schlaefer, A. (2015). *Creating 3D gelatin phantoms for experimental evaluation in biomedicine, 1*(1), 331–334.

Suo, H., Zhang, D., Yin, J., Qian, J., Wu, Z. L., & Fu, J. (2018). Interpenetrating polymer network hydrogels composed of chitosan and photocrosslinkable gelatin with enhanced mechanical properties for tissue engineering. *Materials Science and Engineering: C, 92*, 612–620.

Vincent, J. F. V., & Wegst, U. G. K. (2004). Design and mechanical properties of insect cuticle. *Arthropod Structure & Development, 33*(3), 187–199.

Xie, F. (2023). Chapter 4 - 3D printing of biopolymer-based hydrogels. In M. Mehrpouya, & H. Vahabi (Eds.), *Additive manufacturing of biopolymers* (pp. 65–100). Elsevier.

Xu, C., Chai, W., Huang, Y., & Markwald, R. R. (2012). Scaffold-free inkjet printing of three-dimensional zigzag cellular tubes. *Biotechnology and Bioengineering, 109*(12), 3152–3160.

Zheng, B., Tang, Y., Xie, F., & Chen, L. (2022). Effect of pre-printing gelatinization degree on the structure and digestibility of hot-extrusion 3D-printed starch. *Food Hydrocolloids, 124*, Article 107210.